Hip Implant Design With Three-Dimensional Porous Architecture of Optimized Graded Density

Yingjun Wang
National Engineering
Research Center of Novel Equipment
for Polymer Processing,
The Key Laboratory of Polymer Processing
Engineering of the Ministry of Education,
School of Mechanical
and Automotive Engineering,
South China University of Technology,
Guangzhou 510641, China

Sajad Arabnejad
Department of Mechanical Engineering,
McGill University,
Montreal, QC H3A0C3, Canada

Michael Tanzer
Jo Miller Lab,
Division of Orthopaedic Surgery,
McGill University,
Montreal, QC H3G 1A4, Canada

Damiano Pasini[1]
Department of Mechanical Engineering,
McGill University,
Montreal, QC H3A0C3, Canada
e-mail: damiano.pasini@mcgill.ca

Even in a well-functioning total hip replacement, significant peri-implant bone resorption can occur secondary to stress shielding. Stress shielding is caused by an undesired mismatch of elastic modulus between the stiffer implant and the adjacent bone tissue. To address this problem, we present here a microarchitected hip implant that consists of a three-dimensional (3D) graded lattice material with properties that are mechanically biocompatible with those of the femoral bone. Asymptotic homogenization (AH) is used to numerically determine the mechanical and fatigue properties of the implant, and a gradient-free scheme of topology optimization is used to find the optimized relative density distribution of the porous implant under multiple constraints dictated by implant micromotion, pore size, porosity, and minimum manufacturable thickness of the cell elements. Obtained for a 38-year-old patient femur, bone resorption is assessed by the difference in strain energy between the implanted bone and the intact bone in the postoperative conditions. The numerical results suggest that bone loss for the optimized porous implant is only 42% of that of a fully solid implant, here taken as benchmark, and 79% of that of a porous implant with uniform density. The architected hip implant presented in this work shows clinical promise in reducing bone loss while preventing implant micromotion, thereby contributing to reduce the risk of periprosthetic fracture and the probability of revision surgery. [DOI: 10.1115/1.4041208]

Keywords: total hip arthroplasty, cellular material, proportional topology optimization, asymptotic homogenization, fatigue analysis

1 Introduction

As an effective treatment for osteoarthritis, total hip arthroplasty (THA) is successfully performed every year on over one million patients, a number that is projected to double within the next two decades [1]. Even in a well-functioning total hip replacement, significant peri-implant bone resorption can occur as a result of a number of factors including stress shielding and wear debris [2]. In this work, we focus on bone resorption secondary to stress shielding, and we do not consider wear debris despite its role in promoting macrophages that trigger osteoclasts and initiate bone resorption around the implant, thus resulting in loss of implant fixation [3]. Ideally, periprosthetic stress shielding should be avoided after primary THA so as to minimize the risk of subsequent periprosthetic fracture and/or complications at the time of revision surgery. Although the survivorship of THA exceeds 95% with a more than 10-yr follow-up [4,5], over 15% of hip prostheses still require revision surgeries [6–8], and approximately half of revisions occur in less than 5 years [9]. Revision surgery is a much more complex procedure than primary THA due to bone loss around the prosthesis, which increases the complexity of revision surgery along with its failure rate. Revision surgery is associated with a tenfold increased risk of prosthetic fracture with cemented prostheses and a fourfold increase with cementless prostheses [1].

The cause for bone resorption secondary to stress shielding is that current orthopedic prostheses are made of solid metals, e.g., titanium-based alloys, cobalt chromium alloys, 316 L stainless steel, and tantalum, that are much stiffer than the bone surrounding them [10]. When the hip is loaded during gait or other physical activities, the stiffer prosthesis is prompt to absorb a substantial percentage of stress, thereby leaving only a smaller portion of load transfer to the adjacent bone, which is in turn shielded. In the past, composite materials with a low modulus of elasticity were introduced with the goal of reconciling the elastic property mismatch between the implant and the adjacent host bone [11–13]. The results were not as promising due to the poor strength and long-term durability that those implants would provide under cyclic loadings [13,14]. In addition, softer materials, e.g., carbon fibers, used for hip replacement in the past resulted in clinical complications, such as macrophages formation and transport to the lymphatics with subsequent undesired circulation through the vascular system [15].

Besides solids and composites, porous materials are commonly used in orthopaedic implants, with the main purpose of promoting bone tissue ingrowth and fixing the implant in the long term [16,17]. So far, however, their use for load-bearing applications has been very sporadic. Whereas conventional machining processes have shown limitations in building parts with complex porous architecture, recent technology for additive manufacturing (AM), such as selective laser melting (SLM), selective laser sintering, and electron beam melting, gives far more design freedom to customize structures at the microscale with complex geometry. For example, Pattanayak et al. [18] used SLM to fabricate pure Ti porous parts with microstructure analogous to human cancellous bone, porosity of 55–75% and compressive strength in the range 35–120 MPa. Cheng et al. [19] used selective laser sintering to produce Ti_6Al_4V materials with varying porosity that structurally mimicked the trabecular bone of humans. Li et al. [20] utilized electron beam melting to fabricate porous Ti_6Al_4V parts for biomedical applications. The implants feature porous microarchitecture with uniform porosity of 66% and elastic modulus of only 2.5 GPa, a value close to that of human cancellous bone. Bandyopadhyay et al. [21] used laser engineered net shaping (LENS^{TM}) to build porous Ti_6Al_4V alloy structures with porosity in the range of 18–32%. The modulus of elasticity varied between 7 and 60 GPa, and a 0.2% offset yield strength between 471 and

---

[1]Corresponding author.

809 MPa was adopted. All the biomedical implants cited above are cellular with uniform pore distribution, a factor that makes them unable of matching the graded porosity and elastic moduli variation that occur in human bones. Further work on additive manufacturing of porous metals for orthopaedic implants can be found in a recent review paper [22], which also examines the state of the art of topological design for porous metals.

Reducing bone resorption secondary to stress-shielding has been the goal of a number of papers for more than 20 years. Kuiper and Huiskes [23,24] were the first to optimize the two-dimensional distribution of the elastic modulus for minimum bone loss and probability of interface failure. Gross and Abel [25] worked on the optimization of a hollow stemmed hip implant with the goal of reducing stress shielding and controlling the maximum stress in the cement, and the minimum stress in the bone tissue. Both these works resorted to oversimplified analyses, with a primitive geometry for implant and femur as well as inaccurate loadings and constraint conditions. Hedia et al. [26] attempted to reduce stress shielding by designing a hip stem with three distinct constituents, hydroxyapatite, bioglass, and collagen, materials that are brittle with insufficient strength, hence having limited clinical use. Fraldi et al. [27] used topology optimization for maximum stiffness of a femur-implant assembly with the goal of reducing stress shielding. A map of apparent densities obtained within the prosthesis domain was presented to offer design guidelines, whereas laser drilling was suggested to generate the required microporosity. The choice of maximum stiffness as objective function in their work is questionable, since only a reduction in implant stiffness can decrease stress shielding. Besides the works cited above, there are other approaches in the literature that use shape optimization to streamline the outer boundary of the implant macrogeometry [28–32].

In the recent past, a methodology was proposed for the design of a hip implant with a graded cellular material [10]. An approach combining multiscale analysis and structural optimization was proposed to optimize the implant density distribution for reduced bone resorption and bone–implant interface stress, the latter limiting implant micromotion within an admissible value. The method was applied to a planar domain that represents the implanted femur, and optimization was achieved via an evolutionary algorithm. Later, the fatigue design of the implant as well as its in vitro performance testing were also addressed with the purpose of improving its service life, another critical issue for hip implants that are fully porous [33–35]. In these contributions, the design domain was considered as planar, and the evolutionary scheme used to find trade-off density distributions was time consuming with outcome that might not necessarily lead to the most promising solution [36]. All these issues are here addressed.

This paper examines a fully three-dimensional (3D) domain of the implanted femur subjected to multiple design constraints, and presents a time-efficient computational scheme to optimally grade the spatial distribution of its relative density. To solve the large-scale 3D problem, we use a recently introduced scheme for topology optimization, the proportional topology optimization (PTO) [37], to minimize one objective function, i.e., bone resorption, and convert the other, i.e., bone–implant interface failure, into a design constraint that prevents bone–implant micromotion. PTO is a gradient-free method chosen here over other stochastic and gradient-based methods, such as solid isotropic material with penalization SIMP [38–41] and level set [42–45], for its simplicity and efficiency. While PTO does not require to calculate the sensitivity of objective function and constraints [46], it does preserve the flexibility to design for intermediate densities, a factor that is relevant to the problem examined here. So far, the PTO has not been used to solve multiscale problems of an architected material domain where cell topology and relative density control the macroscopic response, as tackled in this work. The general procedure to tailor the hip implant architecture is presented in Sec. 2, which is followed by a description of the homogenized mechanical properties of the 3D lattice material. Section 4 describes the extended TO scheme for a 3D hip domain constrained by implant micromotion, bone ingrowth, and manufacturing requirements [34,35,47]. The results of the optimized architecture are given in Sec. 5 for the hip implant, followed by concluding remarks with suggestions for future work.

2 Optimization Scheme for Graded-Density Hip Implant With Cellular Material

Computationally designed implants with optimally graded density of cellular material involve multiscale mechanics and structural optimization subject to multiple constraints on pore size, porosity, and strut thickness along with restrictions on the allowable level of implant micromotion [34,35]. Figure 1 shows the main steps of the workflow followed here to solve the constrained optimization problem. Finite element (FE) analysis (ANSYS, Canonsburg, PA) is used to retrieve the mechanical properties of the implant at each iteration. The PTO [37] is here extended to solve a problem where constraints of pore size, porosity, and strut thickness are converted into lower and upper bounds of element density, with two density-update strategies constructed ad hoc to handle the interface failure and fatigue constraints. The interface failure constraint is also introduced to prevent bone–implant micromotion, and the fatigue constraint is applied to the microlattice structure to guarantee the strength necessary to sustain the physiological set of mechanical loadings. The following is a description of the main steps:

(1) A CAD model is created by processing CT-scan data from the femur of a 38-yr-old patient. Two numeric models are then generated, one for the intact femur and the other for the implanted femur, as described in Sec. 3.3. The difference in strain energy density between the two is used as a proxy for bone resorption (details in Sec. 5).

(2) The implant macrogeometry has a minimally invasive shape that is clinically relevant to current THA, whereas a tetrahedron-based topology defines the unit cell, although other cell topologies can be used too. Used to tessellate the 3D implant domain (Fig. 2), this cell is selected for its ease in mapping smoothly from the numeric mesh of the FE model. Its relevant properties, e.g., the effective elastic moduli and the yield surfaces under multi-axial loadings, are obtained via asymptotic homogenization (AH), as described in detail in Sec. 3.1 [34,35,48]. Figure 2 shows the unit cell geometry obtained as an assembly of tetrahedra, where p is the pore size, and t is the cell wall thickness; its mechanical properties, manufacturability via additive process as well as bone-in growth have been recently examined and proved to be suitable for load-bearing bone replacement implants [34,35,49]. Its relative density ρ is the volume fraction, given by the volume ratio of the solid material, V_s, and the unit cell, V, as

$$\rho = V_s/V \qquad (1)$$

(3) The homogenized properties are assigned to the numerical model to build the global stiffness matrix, which in turn is used to solve the boundary value problem. As a result, the strains and stresses of both bone and implant are retrieved to calculate the difference in strain energy density between intact and implanted femur, a figure of merit that indicates bone resorption (Sec. 5).

(4) A multiconstraint TO scheme that extends the previously introduced PTO [37] is used to optimize the relative density distribution of the elements that are associated to the 3D domain of the implanted femur. In particular, minimum bone resorption is converted into maximum compliance, and the problem is solved to yield a density-continuous distribution. To prevent bone–implant micromotion, an additional constraint is applied to the interface failure. At each
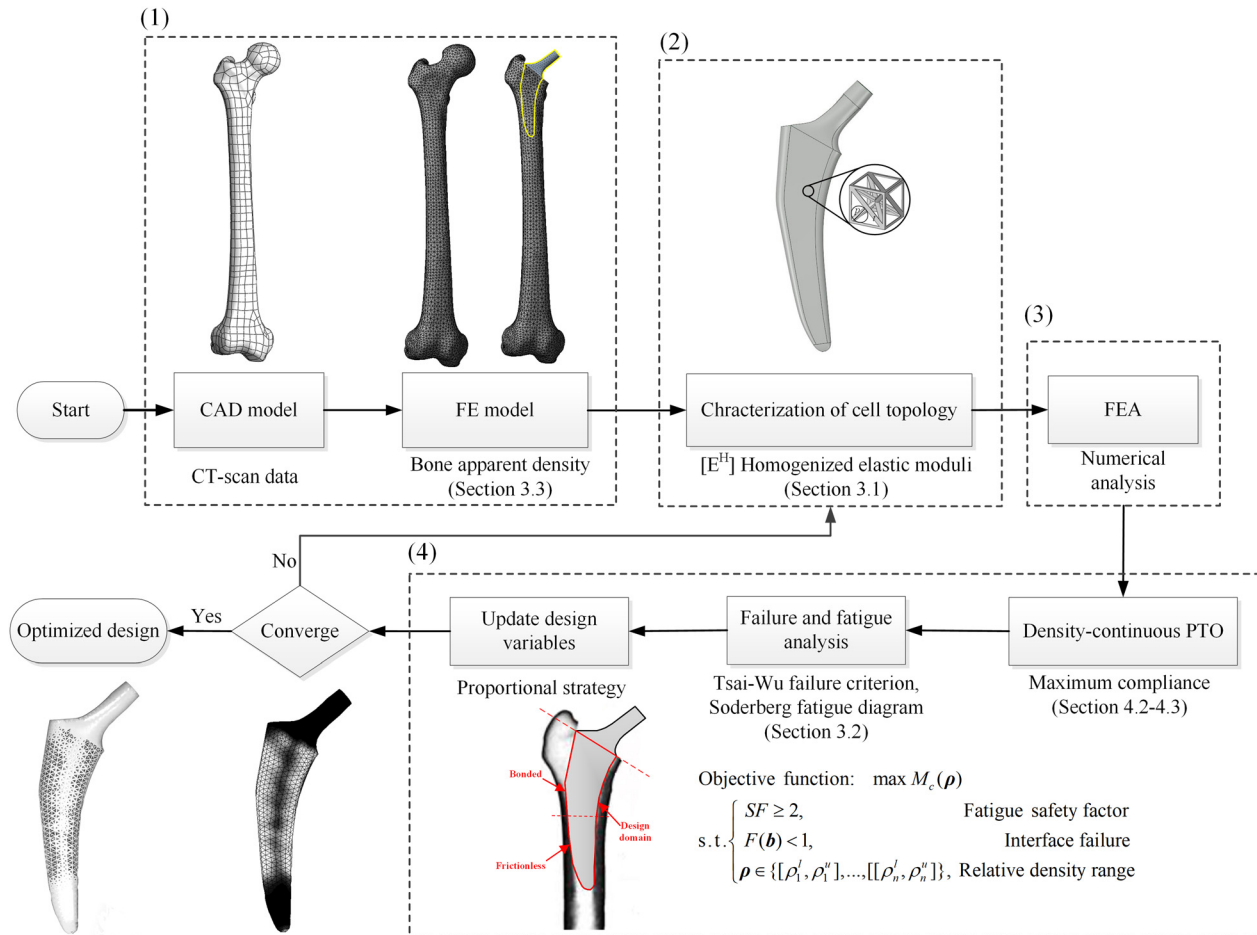
Fig. 1 Flow chart of the multiscale multiconstraint PTO followed in this work for the 3D design of the hip implant

iteration, failure and fatigue analyses are performed, and the design variables are updated to guarantee the necessary level of strength for the implant under service physiological conditions. In addition, the constraints of average porosity, pore size, and minimum cell wall thickness that can be manufactured with current additive technology are converted into lower and upper bounds of relative density; hence, they are directly taken into account during the optimization process [10]. The optimal density distribution is obtained upon convergence of the modified TO. The details of the TO scheme are given in Secs. 4.2–4.3, and the failure analyses are presented in Sec. 3.2.

Finally, once the optimal relative density distribution is obtained, an in-house code is used to automatically generate the 3D lattice distribution of the implant via Rhinoceros (Seattle, WA). Appendix A includes the main steps for the lattice generation. Since the manufacturing requirements identified in previous works are here integrated in the problem formulation, the final cellular architecture can be additively built with a satisfactory level of accuracy that satisfies both bone ingrowth requirements and manufacturing constraints [48,49].

3 Mechanics of Lattice Materials

3.1 Homogenized Properties. A fully resolved resolution of a large lattice domain with explicit modeling of its microstructural features can be very lengthy and time-consuming. Homogenization schemes have been introduced to calculate the effective properties of a heterogeneous material in terms of the properties of the representative volume element [50]. In this work, the lattice material is replaced by an equivalent homogeneous solid with effective properties that are here determined via AH applied to the unit cell [51]. The effective stiffness tensor E_{ijkl}^H of the lattice are then calculated as
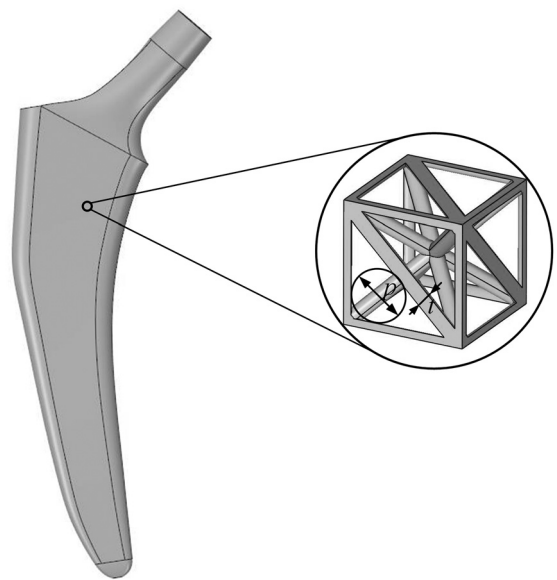

Fig. 2 Macrodomain and building block for generating the lattice architecture of the hip implant
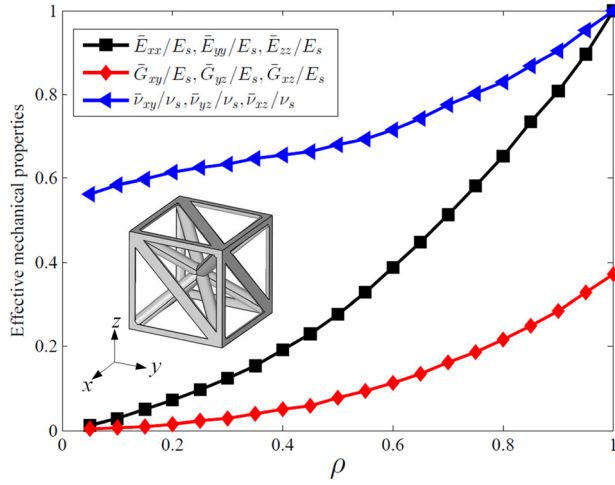
Fig. 3 Effective mechanical properties of tetrahedron-based unit cell; E_s is the elastic modulus of the fully solid material

$$E_{ijkl}^H = \frac{1}{|V|} \int_{V_s} E_{ijmn} M_{mnkl} dV \qquad (2)$$

where $|V|$ is the volume of the entire unit cell, V_s is the solid part of the cell, E_{ijkl} is the local elasticity tensor which equals to the elasticity tensor of the solid material and equals to zero for a void domain. M_{ijkl} is the local structure tensor that correlates the macroscopic strain $\bar{\varepsilon}_{ij}$ to the microscopic strain ε_{ij} as

$$\varepsilon_{ij} = M_{ijkl} \bar{\varepsilon}_{ij} \qquad (3)$$

and M_{ijkl} is calculated as

$$M_{ijkl} = \frac{1}{2} \left(\delta_{ik} \delta_{jl} + \delta_{il} \delta_{jk} \right) - \varepsilon_{ij}^{*kl} \qquad (4)$$

where δ_{ij} is the Kronecker delta, and ε_{ij}^{*kl} is the microstructural strain corresponding to the component kl of the macroscopic strain $\bar{\varepsilon}_{ij}$. More details about the calculation of ε_{ij}^{*kl} can be found in Ref. [52]. The microscopic stresses can be written as

$$\sigma_{ij} = E_{ijkl} M_{klmn} \bar{\varepsilon}_{mn} = E_{ijkl} M_{klmn} [(E_{pqmn}^H)^{-1} \bar{\sigma}_{pq}] \qquad (5)$$

The von Mises stress distribution over the microstructure is then used to capture the yield surface of the unit cell, which is expressed as

$$\bar{\sigma}_{ij}^y = \frac{\sigma_{ys}}{\max\{\sigma_{vM}(\bar{\sigma}_{ij})\}} \bar{\sigma}_{ij} \qquad (6)$$

where $\bar{\sigma}_{ij}^y$ is the yield strength of the unit cell, σ_{ys} is the yield strength of the bulk material, and $\sigma_{vM}(\bar{\sigma}_{ij})$ is the von Mises stress of the microstructure corresponding to the macroscopic stress $\bar{\sigma}_{ij}$. At each iteration, AH is used to obtain the effective mechanical properties and relative density of each element. To avoid repeated AH computations and speed up the simulations within the optimization loop, we compute a priori the effective mechanical properties as a function of the relative density range [0, 1]. Figure 3 shows the effective elastic modulus, $\bar{E}_{ii}$, shear modulus, $\bar{G}_{ii}$, and Poisson's ratio, $\bar{v}_{ij}$ of the unit cell (Fig. 2) which has cubic symmetry. Table 1 shows the fitting functions obtained through the least squares method, where R-squared (R^2) indicates how accurately the data fit the function [53]. An R^2 of 1 indicates that the function perfectly fits the data, whereas $R^2 = 0$ is the worse fit. These expressions are directly used during the optimization process, thereby avoiding resorting to AH at each iteration.

Table 1 Effective mechanical properties of tetrahedron-based unit cell as a function of relative density

	Fitting function	R-squared (R^2)
$\dfrac{\bar{E}_{xx}}{E_s} = \dfrac{\bar{E}_{yy}}{E_s} = \dfrac{\bar{E}_{zz}}{E_s}$	$0.8861\rho^2 + 0.0928\rho + 0.0127$	0.9998
$\dfrac{\bar{G}_{xy}}{E_s} = \dfrac{\bar{G}_{yz}}{E_s} = \dfrac{\bar{G}_{xz}}{E_s}$	$0.4517\rho^2 - 0.1043\rho + 0.0154$	0.9984
$\dfrac{\bar{v}_{xy}}{v_s} = \dfrac{\bar{v}_{yz}}{v_s} = \dfrac{\bar{v}_{xz}}{v_s}$	$0.5352\rho^3 - 0.4307\rho^2 + 0.3466\rho + 0.5526$	0.9988

3.2 Fatigue Failure of Lattice Materials. Since the femur is typically subjected to a combination of multidirectional loads that vary cyclically with time and direction [54,55], it is essential to develop expressions that predict the multiaxial failure of the hip implant. For this purpose, we adopt here the Tsai-Wu failure criterion [56], one candidate criterion for multiaxial failure that is typically used for composite materials and also for trabecular bone.

The Tsai-Wu failure criterion can be expressed in terms of $\bar{\sigma}_i$ as

$$F_i \bar{\sigma}_i + F_{ij} \bar{\sigma}_i \bar{\sigma}_j \leq 1 \qquad (7)$$

where $i, j = 1, \ldots, 6$ and $\bar{\sigma}_i$ are the stress components expressed in Voigt notation, and F_i and F_{ij} are coefficients generally determined from equibiaxial tests.

The tetrahedron-based unit (Fig. 2) here used has three planes of symmetry such that $F_{ij} = F_{ji}$. In addition, the proposed base material is Ti$_6$Al$_4$V, which is biocompatible, additively manufacturable, and commonly used in orthopedics, with almost equal tensile and compressive yield strengths, i.e., $F_i = 0$. Hence, Eq. (7) can be expanded and reduced to

$$F_{11}\bar{\sigma}_1^2 + F_{22}\bar{\sigma}_2^2 + F_{33}\bar{\sigma}_3^2 + F_{44}\bar{\sigma}_4^2 + F_{55}\bar{\sigma}_5^2 + F_{66}\bar{\sigma}_6^2$$
$$+ 2F_{12}\bar{\sigma}_1\bar{\sigma}_2 + 2F_{13}\bar{\sigma}_1\bar{\sigma}_3 + 2F_{23}\bar{\sigma}_2\bar{\sigma}_3 \leq 1 \qquad (8)$$

Assuming for uniaxial tension that the yield strength along the three principal directions is $\bar{\sigma}_1^y$, $\bar{\sigma}_2^y$, and $\bar{\sigma}_3^y$, and the shear strength in the three planes of symmetry is $\bar{\sigma}_4^y$, $\bar{\sigma}_5^y$, and $\bar{\sigma}_6^y$, we can write

$$F_{ii} = \frac{1}{(\bar{\sigma}_i^y)^2}, \quad i = 1, \ldots, 6 \qquad (9)$$

As previously written, the coefficients F_{12}, F_{13}, and F_{23} can be determined via equibiaxial tests. If the failure strength in equibiaxial tension are $\bar{\sigma}_1 = \bar{\sigma}_2 = \bar{\sigma}_{b12}^y$, $\bar{\sigma}_1 = \bar{\sigma}_3 = \bar{\sigma}_{b13}^y$, $\bar{\sigma}_2 = \bar{\sigma}_3 = \bar{\sigma}_{b23}^y$ then Eq. (9) reduces to

$$F_{ij} = \frac{1}{2(\bar{\sigma}_{bij}^y)^2} \left[1 - (\bar{\sigma}_{bij}^y)^2 (F_{ii} + F_{jj}) \right], \quad i,j = 1, \ldots, 3 \text{ and } i \neq j \qquad (10)$$

To design the lattice material against fatigue failure under multiaxial loadings, the Soderberg criterion can be used such that

$$\frac{\|\bar{\sigma}^m\|}{\|\bar{\sigma}^y\|} + \frac{\|\bar{\sigma}^a\|}{\|\bar{\sigma}^e\|} = \frac{1}{SF} \qquad (11)$$

where $\|\ \|$ denotes the second norm of the vector, and $\bar{\sigma}^m$ and $\bar{\sigma}^a$ are the mean and alternating macroscopic stresses given by

$$\bar{\sigma}^m = \frac{\bar{\sigma}^{max} + \bar{\sigma}^{min}}{2}, \bar{\sigma}^a = \frac{\bar{\sigma}^{max} - \bar{\sigma}^{min}}{2} \qquad (12)$$

where $\bar{\sigma}^{max}$ and $\bar{\sigma}^{min}$ are the multiaxial macroscopic stresses that cause the highest and lowest values of the von Mises stress in the

microstructure. The yield strength $\bar{\sigma}^y$ is calculated through Eq. (6) and the endurance limit is obtained as

$$\bar{\sigma}^e = \bar{\sigma}^y \frac{\sigma_{es}}{\sigma_{ys}} \qquad (13)$$

where σ_{ys} and σ_{es} are, respectively, the yield strength and the endurance limit of the bulk material. More details can be found in Refs. [33] and [48].

3.3 Numerical Model. Figure 4(a) shows the 3D reconstruction of the femur from the CT scan data of a 38-yr-old male patient, taken from a dataset of last-generation imaging with resolution lower than modern CT scans. Inhomogeneous material properties of the bone tissue (Fig. 4(b)) are mapped to each voxel via an in-house algorithm that converts the Hounsfield units (HU) into the elastic modulus (E) using user-defined parameters. In this work, the effective density of 1.0 g/cm³ for water at 0 HU is assigned to an apparent density $\rho = 0$ g/cm³, and the maximal HU value, which corresponds to the densest region of the cortical bone, is set to an apparent density of 2.0 g/cm³ (Fig. 4(b)) [33]. The bone apparent density represents the density of solid bone excluding the density of the fluid mass, namely the density of blood. On the other hand, the bone effective density accounts for the fluid mass. The relationship between apparent density and HU is assumed as linear, hence, the effective elastic moduli of the bone can be obtained as [57,58]

$$\begin{cases} E = 1904\rho^{1.64} & \rho \le 0.95 \\ E = 2065\rho^{3.09} & \rho > 0.95 \end{cases} \qquad (14)$$

Figure 4(c) shows the boundary and loading conditions applied to the FE model, where the distal end is fully fixed, and the X and Y displacements of the condyle are constrained. The loads (unit: N) written in the (X, Y, Z) coordinate system, are F_1 (−486, −295.2, 2062.8), F_2 (64.8, 104.4, −118.8), F_3 (522, 38.7, −778.5), F_4 (−4.5, −6.3, 171), and F_5 (−8.1, 166.5, 836.1), and the loading locations (unit: m) are P_1 (0.035, 0.009, −0.449), P_2 (−0.039, −0.018, −0.41), P_3 (−0.022, −0.01, −0.375), and P_4 (0, 0, 0) [48]. Two FE models are generated, one for the intact femur and the other for the implanted femur. For the implant design, the hip stem is subjected to physiological loading and boundary conditions during the gait cycle that were obtained from in vivo measurements on an instrumented hip [48,59,60]. In particular, one specific patient and musculoskeletal load profile are here adopted, as an exemplary case. This set represents the single instant of maximum contact force of the hip in each of the walking and stair climbing cycles of a given patient; the maximum contact force coincides with the peak anterior–posterior force, a value that represents also the load profile for maximum torsion acting on the shaft of the implant [59].

In this work, we select for the implant geometry that of the Trilock implant (Warsaw, IN), because it clinically provides an excellent metaphyseal fixation to the proximal femur [61,62]. The 3D geometry of the Trilock implant is thus prescribed to define the design domain within the femur (Fig. 5). To prevent the occurrence of bone–implant micromotion, an interface stress constraint is applied during the optimization scheme. The implant is considered as fully bonded in the upper part of the implant and femur. The fully bond assumption represents the condition in which bone ingrowth occurs at the interface of the proximal region of the stem, which is porous with pore size and porosity tailored to meet bone ingrowth requirements [34]. Bone tissue grows into the cellular portion of the implant months after the operation, thus providing implant stability and fixation. A frictionless contact is applied to the lower part of the implant and the femur (below the
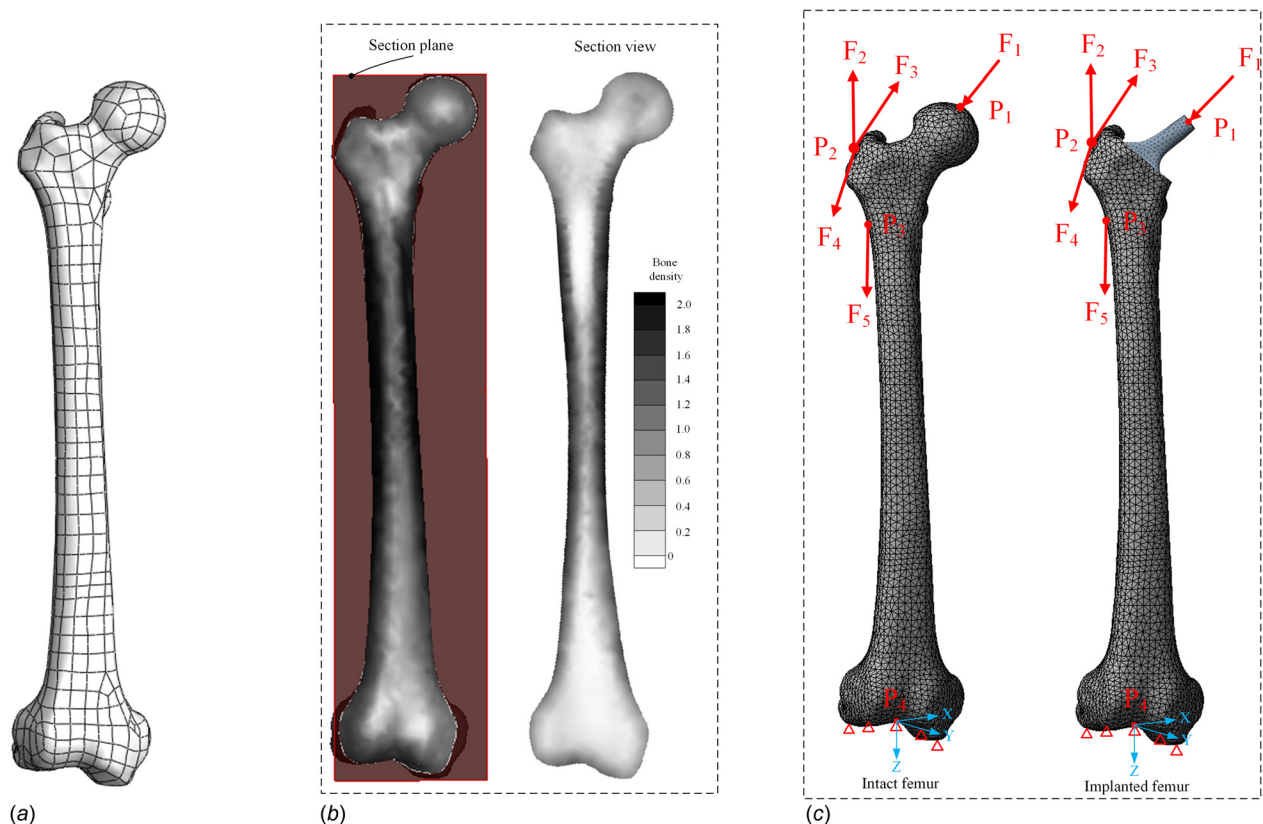

Fig. 4 Three-dimensional femur model of a 38-year-old male patient: (a) CAD model, (b) physical model of bone apparent density, and (c) FE model with relevant physiological loadings and boundary conditions obtained from in vivo measurements on an instrumented hip [48,59,60]
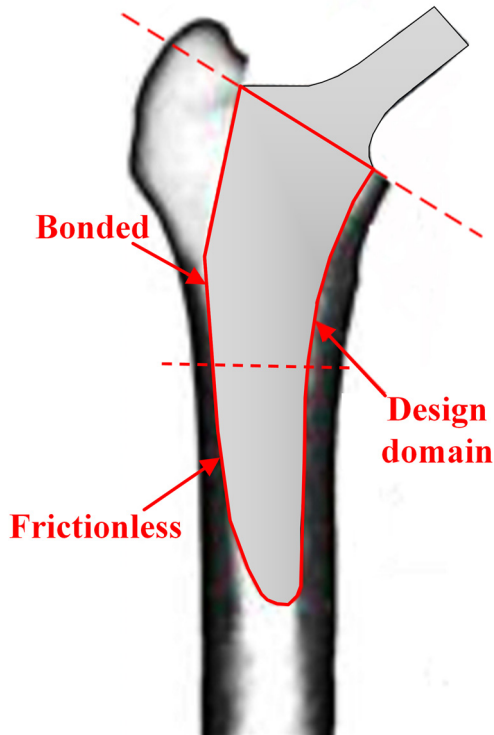
Fig. 5 Design domain of the hip implant within the femur

horizontal dash line in Fig. 5) to satisfy boundary and loading conditions.

4 Multiconstraint Topology Optimization

4.1 Objective Function and Design Variables. Current orthopedic prostheses are generally made of metals, such as 316 L stainless steel, cobalt chromium alloys, titanium-based alloys, and tantalum [10]. These solids are generally much stiffer than the host bone tissue, e.g., the elastic modulus of Ti_6AI_4V is 120 GPa but that of the stiffest femur tissue (cortical bone) is only around 19 GPa [63], thereby yielding to stress shielding [6], one major reason for bone resorption.

A decrease in the elastic modulus of the implant can certainly favor stress sharing between implant and femur, thus reducing the likelihood of bone resorption secondary to stress shielding [6]. In this work, the objective of minimizing bone resorption is expressed as the maximization of the implant compliance subject to the relevant constraints. Unlike conventional black-white topology optimization (TO) [64,65], the TO here used optimizes the relative density distribution of all elements associated with the 3D implant domain, which is in turn mapped to a lattice architecture of the implant satisfying the constraints imposed by implant micromotion, additive manufacturing, and bone ingrowth [34,35].

In the numeric formulation, each element of the FE model refers to a unit cell with relative density corresponding to the relative density of the element. By doing so, the element densities represent the design variables, and the density-based TO method can be used to solve the optimization problem. Since the element discretization algorithm cannot guarantee that all elements within the irregular domain of the implant have identical size, lower and upper bounds are selected for the density of each element.

The constraints considered in the optimization refer to bone ingrowth, manufacturing, interface failure controlling implant micromotion and fatigue strengths, as described below:

(a) *Bone ingrowth requirements*: Porosity higher than 50%, and pore size between 50 and 800 μm are applied to the proximal portion of the implant [34,35,66].

(b) *Manufacturing constraints*: Pore wall thickness larger than 200 μm is enforced to respect typical minimum values of strut thickness that can be built with current additive technology [34,35,67].

(c) *Interface failure to prevent implant micromotion*: Interface failure of bone-implant $F(b)$, determined by the local shear stress $\tau(b)$ at point b, is imposed to be below 1 so as to guarantee a low risk of interface failure, with $F(b)$ expressed as [33]

$$F(b) = \tau(b)/(21.6\rho(b)^{1.65}) \qquad (15)$$

where ρ here is the bone density. An increase of shear stress between the implant and the surrounding bone can increase the risk of interface micromotion and instability [68,69]. Hence, Eq. (15) can be used to constrain the shear stress below an allowable value (i.e., $21.6\rho(b)^{1.65}$), that can reduce the risk of bone–implant micromotion. This approach has been shown effective and tested in a previous study [33].

(d) *Lattice fatigue failure*: Safety factor in Eq. (11) should be set above 2 [33] to guarantee the service life of the lattice implant.

To include the constraints (a) and (b) directly in the optimization process, their values are converted into lower and upper bounds of relative density. Failure and fatigue analyses are performed at each iteration, and the design variables are updated to satisfy failure and fatigue requirements, i.e., constraints (c) and (d). The TO problem for maximum compliance $M_c(\boldsymbol{\rho})$ can then be summarized in mathematical terms as

$$\max M_c(\boldsymbol{\rho})$$
$$s.t. \begin{cases} SF \geq 2, & \text{fatigue safety factor} \\ F(\boldsymbol{b}) < 1, & \text{interface failure} \\ \rho \in \left\{ \left[\rho_1^l, \rho_1^u\right], ..., \left[\rho_n^l, \rho_n^u\right] \right\}, & \text{relative density range} \end{cases}$$
$$(16)$$

where ρ_i^l and ρ_i^u are the lower and upper bounds of element i.

As described in the methodology section, the solution of the optimization problem results in optimized elasticity gradients that maximize the stem compliance under a number of constraints including implant–bone interface failure and fatigue failure. These constraints ensure that the implant is not overly compliant, and its optimized properties can also reduce the risk of interface micromotion.

4.2 Proportional Topology Optimization With Continuous Design Variables. The PTO, a simple and efficient nonsensitivity method, has been recently used to solve the classical minimum compliance problem and the stress constrained problem for a solid material [37]. In this paper, the PTO is extended to solve maximum compliance problem of a lattice domain under multiple constraints including interface failure and fatigue, two constraints that were not previously examined [37].

For the classical minimum compliance problem, PTO globally manages the proportional distribution of the design variables to the element compliance values as

$$\rho_i^{\text{opt}} = \frac{\text{RM}}{\sum_j^N C_j^q v_j} C_i^q \qquad (17)$$

where ρ_i^{opt} is the ith optimized element density, RM is the remaining material amount that will distribute to elements, N is the number of elements, C_i is the ith element compliance, v_j is the jth element volume, and q is the proportion exponent, value between 0.25 and 3, which controls the degree of proportion between the element density values and the compliance values [37]. After the optimized element density is obtained at each iteration, the new element density is updated as

$$\rho_i^{\text{new}} = \alpha\rho_i^{\text{prev}} + (1-\alpha)\rho_i^{\text{opt}} \qquad (18)$$

where ρ_i^{new} is the ith element density to be used in the next iteration, ρ_i^{prev} is the ith element density from the previous iteration, and α is the history coefficient. From previous findings on the compliance problem, the proportion exponent, q, and history coefficient, α, are set to 1 and 0.5 [37]. We also note that in this work we do not follow the original PTO in defining a priori the penalization factor for the relationship between the Young's modulus and the element density [37], as this choice affects the quality of the solutions as shown in the Appendix B. Rather at each iteration we use the fitting functions in Table 1 that represent the effective mechanical properties of each element of the numerical model.

4.3 Problem Formulation for Topology Optimization of Hip Implant.
For the hip implant optimization, the interface failure and fatigue are included in the PTO formulation, here amended from the original version through the modifications described later.

Since maximum compliance is the objective function used to optimize the material distribution of the hip implant, the material relative density is set proportional to the removed material $(M - RM)$; hence, the proportional material distribution scheme, Eq. (17), is rewritten as

$$\rho_i^{\text{opt}} = \frac{M - \text{RM}}{\sum_j^N C_j^q v_j} C_i^q \qquad (19)$$

where M is the total material amount and the other symbols have the meaning of those describing Eq. (17).

For the failure and fatigue analysis, since the design variables (element relative density) are updated in the density-continuous PTO with constraints on bone ingrowth and manufacturing requirements, the homogenized mechanical properties, which also include yield and fatigue, are recalculated at each iteration for all elements. To update the design variables, two proportional strategies are proposed, where the relative density is adjourned with respect to the safety factors for interface failure (F) and fatigue (SF), respectively, as described here

$$\rho_i^{\text{new}} = \begin{cases} \max\left(\rho_i^l, \dfrac{\rho_i}{\max(\text{NLF}_i)}\right), & \max(\text{NLF}_i) > 1 \\ \rho_i, & \max(\text{NLF}_i) \le 1 \end{cases} \qquad (20)$$

and

$$\rho_i^{\text{new}} = \begin{cases} \min\left(\rho_i^u, \rho_i \dfrac{2}{SF_i^{\text{fatigue}}}\right), & SF_i^{\text{fatigue}} < 2 \\ \rho_i, & SF_i^{\text{fatigue}} \ge 2 \end{cases} \qquad (21)$$

where ρ_i^l and ρ_i^u are lower and upper bounds of relative density for the ith element; NLF_i is the interface failure set that includes the interface failure for all the femur elements adjacent to the ith element, e.g., if j is the kth neighbor femur element to the ith element, and $\text{NLF}_i(k)$ is the interface failure $F(j)$ which is calculated through Eq. (15); SF is the safety factor for the lattice miscrostructure; and SF_i^{fatigue} is the safety factor obtained from the fatigue analysis (Eq. (11)).

5 Results and Discussion

This section presents results for bone resorption that are in turn used to evaluate the postoperative performance of the implant, an important indicator of bone ingrowth after the THA. We follow here an approach already adopted in the literature for the evaluation of bone resorption [24,48,70]. The amount of bone that is under loaded is assessed post implantation relative to the intact femur. With this approach, bone can be considered locally under loaded if its local strain energy U per unit of bone mass ρ $(S = U/\rho)$ is beneath the local reference value S_{ref}, which is the value of S when no prosthesis is present. However, it has been observed that not all values of underloading leads to resorption, and a certain fraction of underloading (the threshold level s) is tolerated. Bone resorption starts when the local value of S is beneath the value of $(1-s)S_{\text{ref}}$. With this definition, the resorbed bone mass fraction m_r can be obtained from

$$m_r(b) = \frac{1}{M}\int_V f(S(b) - (1-s)S_{\text{ref}}(b))\rho(b)dV \qquad (22)$$

where $m_r(b)$ is bone resorption, M, ρ, and V are the original bone mass, density, and volume, $S(b)$ and $S_{ref}(b)$ are the strain energy of point b obtained from the implanted and intact femurs, respectively, and s is the dead zone which is set to 0.5 [10]. $f(x)$ is a resorptive function equal to 1 if $x < 0$ (i.e., $f = 1$ if $S(b) - (1-s)S_{\text{ref}}(b) < 0$ which means bone resorption appears at point b), and equal to 0 otherwise. We also note that the dead zone region is $[(1-s)S_{\text{ref}}(b), (1+s)S_{\text{ref}}(b)]$, and in principle for $S(b)$ above $(1+s)S_{\text{ref}}(b)$ bone growth occurs, but this portion of bone growth is not captured by Eq. (22) since the stress is not shielded in the portions of the femur where bone resorption does not take place. On the other hand, Eq. (22) is used to calculate bone loss for the PTO optimized implant and two baseline implants: one made of fully solid material and the other made of a lattice with uniform density. We note that bone resorption is the result of bone remodeling, an evolving process that occurs over time. In this work, a simplified scheme is adopted, where the actual balance between bone resorption and bone deposition is not accounted for. Further work is needed to implement a more realistic evaluation of bone response as well as to refine the underlying model assumptions.

In the problem formulation, the objective function is to maximize the implant compliance for a volume ratio of 0.5; the initial volume ratio is set to 1 which represents the initial conditions of uniformly solid. Convergence is reached when the following criterion is satisfied

$$\frac{\sum_{i=1}^N (C_{k-i+1} - C_{k-N-i+1})}{\sum_{i=1}^N C_{k-i+1}} < \varepsilon \qquad (23)$$

where C is the objective function value, k is the number of the current iteration, ε is a preset convergence error, and N is an integer number that are, respectively, set to 0.001 and 5, as previously suggested [71].
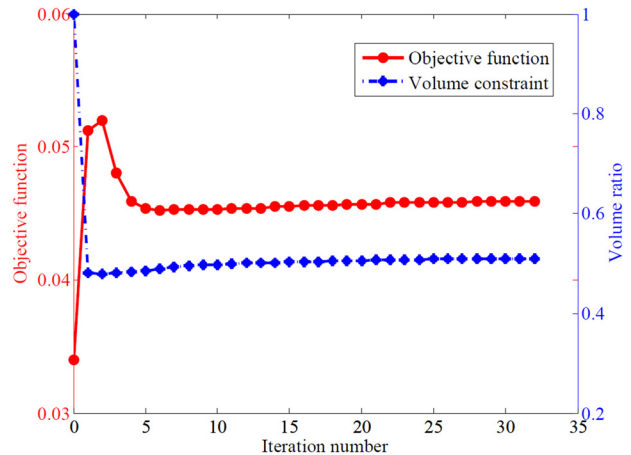

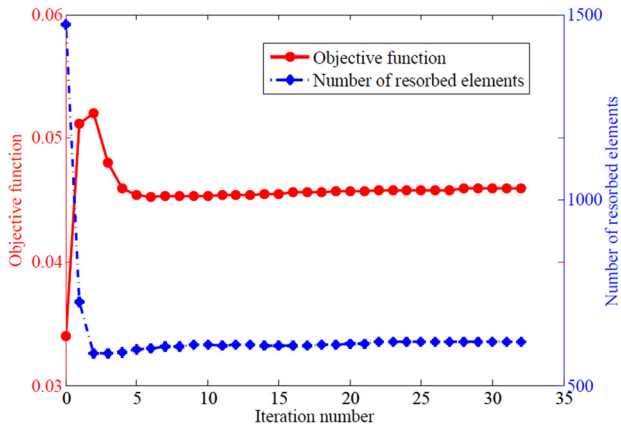
Fig. 6 Convergence history of the hip stem optimization

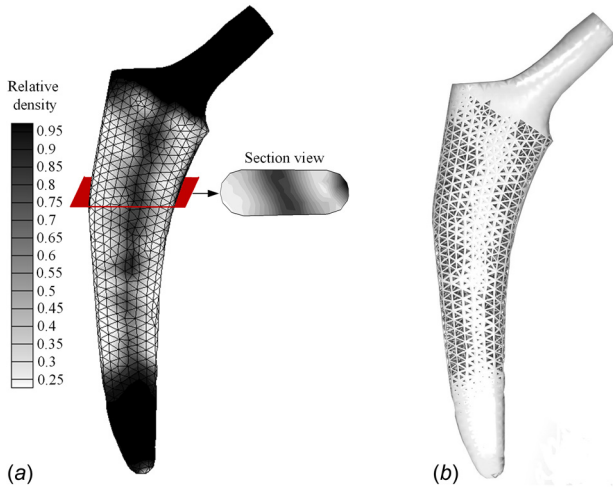**Fig. 7 Relationship between objective function and bone resorption**

(a)

(b)

Fig. 8 The TO results of the implant: (a) optimized gradients of relative density with zoom (besides) of the implant cross section taken through the plane shown in red and (b) corresponding 3D architecture of the porous stem

As shown in the convergence history plotted in Fig. 6, the number of iterations needed to reach convergence is 33. After a small number of iterations, the values of the objective function start to decrease, while the constraints guaranteeing mechanical performance and implant manufacturability gradually take effect. After about 15 iterations, the objective function is 98.6% close to the convergence value. Furthermore, Fig. 7 illustrates the relationship between objective function and bone resorption. The number of resorbed elements increases with the objective value and the trend corroborates the choice of maximizing compliance in the problem formulation subject to the necessary inequality constraints on the strength requirements.

Figure 8(a) shows the optimized relative density distribution, and Fig. 8(b) shows the graded lattice obtained with an in-house code (Appendix A) that creates a lattice architecture that respects bone ingrowth and additive manufacturing constraints, as demonstrated in previous works [34,48]. Comparing to a preceding work [10], where the time to solve the optimization problem of a two-dimensional implant was almost 3 days [48], the method presented in this paper for a more realistic 3D geometry of the implant needs only 10 min, a factor that shows the superior computational efficiency of the scheme here proposed. From Fig. 8, we observe that high density regions distribute along the main implant axis, in the distal part and in the implant neck. This distribution of relative density provides the fatigue strength required to sustain loadings from daily activities while keeping the implant sufficiently compliant to reduce bone resorption secondary to stress shielding as well as sufficiently stiff to prevent implant micromotion.

Figures 9(a)–9(c) shows a relative performance comparison between the baseline Trilock implant and two cellular implants of identical porosity, but dissimilar density distribution, one uniform (relative density of 0.5), and the other optimally graded (Fig. 8). If S is considered as the baseline of bone resorption for the fully solid implant, we can conveniently gauge the relative benefit between implant designs. Compared to the fully solid implant, the uniform lattice brings a bone loss reduction of 46.8%, and the optimal lattice of 58.1%. Bone resorption of the optimized implant is thus 78.8% of that of the uniform lattice implant, a figure that corresponds to a 21.2% improvement in performance. In addition, Fig. 9(a) shows that bone resorption occurs at Gruen zones 1, 2, 6, and 7, which are greatly reduced in Fig. 9(b) and even further in Fig. 9(c), where bone resorption mostly occurs at Gruen zones 6 and 7. These results show that a flexible implant

Fully solid implant

Uniform lattice implant

Graded lattice implant

Bone resorption: S

Bone resorption: $0.532S$

Bone resorption: $0.419S$

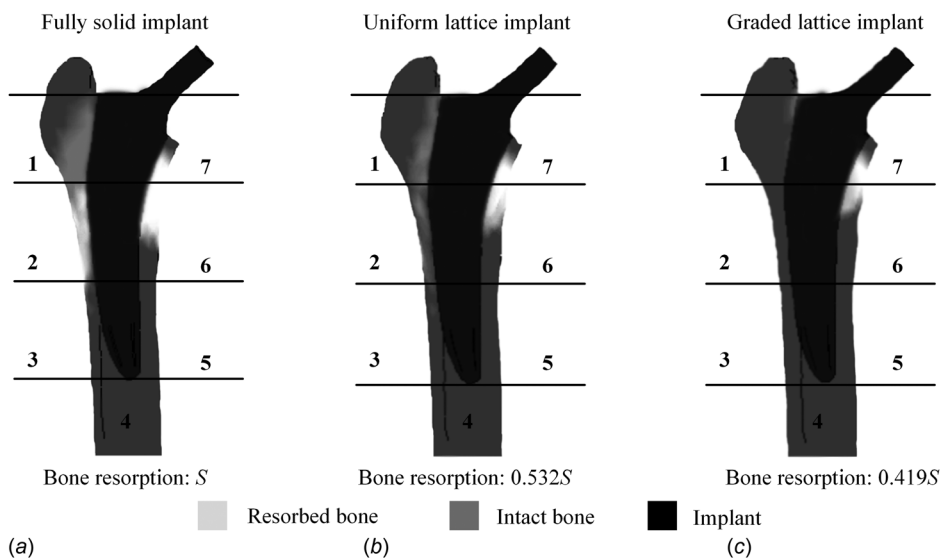Resorbed bone   Intact bone   Implant

(a)   (b)   (c)

Fig. 9 Bone resorption results for: (a) fully solid implant chosen here as baseline, (b) uniform lattice implant with relative density of 0.5, and (c) graded lattice implant, obtained for volume fraction identical to that of the lattice implant with uniform density (Fig. 8(b))

designed for maximum compliance via the TO extended in this work can reduce stress shielding, and hence bone resorption. Furthermore, the graded lattice implant satisfies implant micromotion, failure, and fatigue requirements, besides being able to meet bone ingrowth and manufacturing requirements. Figures 10(a)–10(c) shows the von Mises distribution of the hip implant with fully solid material, uniform porosity, and optimized porosity, respectively. The first one shows the largest area with the highest stress, followed by the other two with the graded density implant achieving the lower value, thus reducing stress shielding. In addition, Figs. 11(a)–11(c) illustrates the von Mises distribution of the femur, which shows a pattern reversed to that of the implant, a result demonstrating that stress shielding is reduced by the implant with optimally graded density.

With respect to the implant manufacture, recent works have demonstrated that AM can successfully build metallic lattice structures including porous implants with complex internal microarchitecture [34,48,72,73]. AM facilitates the fabrication of cellular implants with tailored gradients of porosity and pore morphology that enables bone ingrowth. Investigations on the

impact of manufacturing defects and strategies to mitigate them have been successfully developed for bone replacement implants, thereby demonstrating the feasibility of additively manufacturing the hip implant presented in this work [49]. A proof-of-concept of the implant model shown in Fig. 8(b) is additively built out of Ti_6Al_4V through a SLM 3D printer Laseradd DiMetal-280 (Laseradd, Guangzhou, China). Figure 12 shows the realization where the lattice architecture is generated to satisfy manufacturing and bone ingrowth requirements. In addition, the elastic properties of the solid material printed via SLM are here approximated as isotropic. Local anisotropies at the strut level are disregarded, as corroborated by recent investigations [74]. Because dimensional accuracy and structural properties are strongly correlated in additively built lattice biomaterials [35,74], in this work, the lattice architecture is generated through a compensation strategy that can yield an as-built lattice geometry deviating max 4% from the nominal counterpart [49]. By doing so, the predicted elastic properties are within 10% from the testing data.

The work presented in this study bears limitations that call for follow up investigations. First, the hip stem is here treated as a
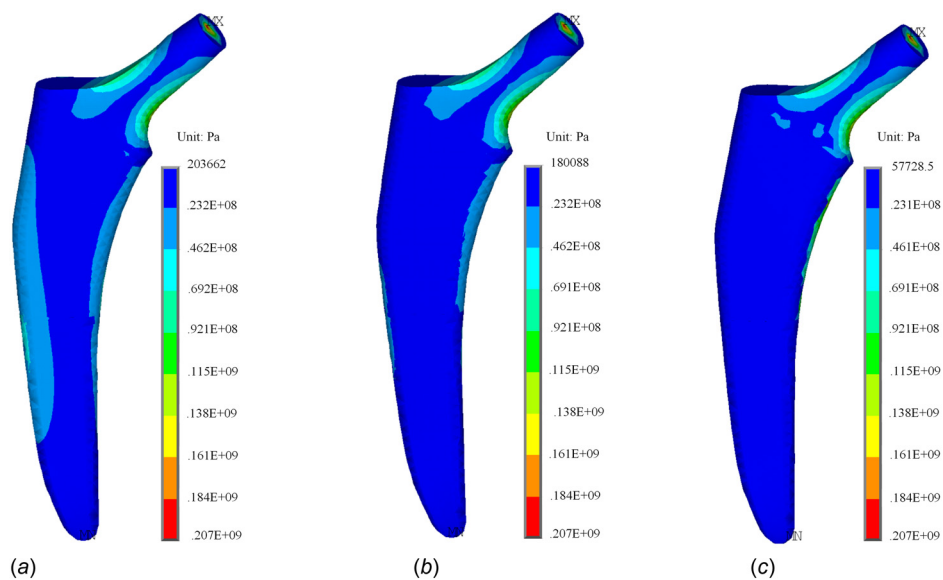

Fig. 10 Von Mises stress of the stem with (a) fully solid material, (b) uniform porosity of 0.5, and (c) optimally graded porosity
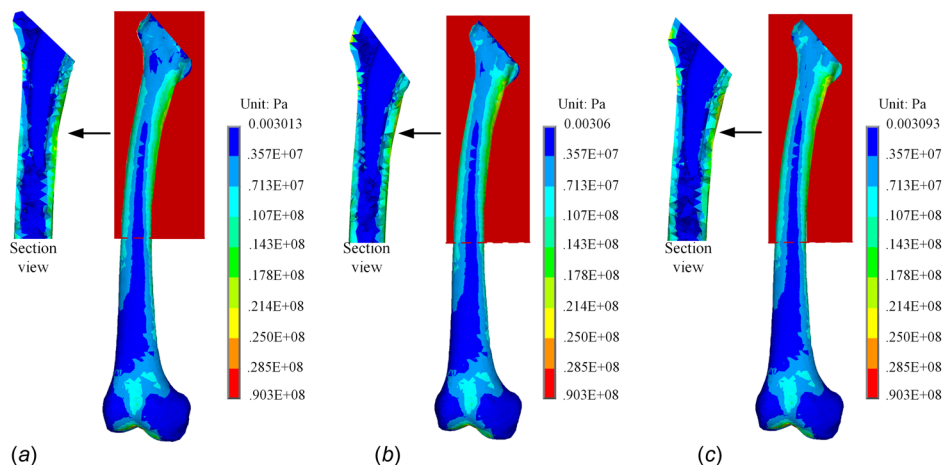

Fig. 11 Von Mises stress distribution in the femoral tissue generated by the following implant designs: (a) fully solid, (b) uniform porosity of 0.5, and (c) optimally graded porosity

6 Conclusions

This paper has extended a gradient-free scheme for topology optimization to tailor the relative density distribution of a hip implant made of a 3D-graded lattice with tetrahedron-based cell topology. Asymptotic homogenization has been used to calculate its elastic, yield, and fatigue properties, expressed as a function of relative density. Multiple constraints have been applied to the implant micromotion, pore size, porosity, and strut thickness, of the lattice architecture so as to satisfy bone ingrowth requirements and the manufacturing limits imposed by current additive technology. The implant performance has been numerically assessed against bone resorption, a figure of merit that describes bone loss secondary to stress shielding. The results given for postoperative conditions, suggests that bone loss for the optimized lattice implant is only 41.9% of that of a fully solid titanium implant. While these findings show promise in contributing to reducing the risk of periprosthetic fracture and the probability of revision surgery, further work is required to validate them through in vitro and clinical models.

Appendix A: Scheme for the Generation of a Graded Lattice

The in-house code developed here for the generation of a graded lattice structure resorts to a representation scheme typically used in computer-aided design (CAD) model. In particular, we adopt the boundary representation (B-rep) for representing a geometric object drawn in a CAD environment [75]. In the B-Rep, information can be topological and geometric. The former provides the relationship of connectivity among vertices, edges, and faces of an object. In addition to connectivity, topological information includes orientation of edges and faces. The latter, i.e., geometric information, describes the actual geometric features of the object, e.g., surfaces, curves, and points, with typical names being face, loop, edge, and vertex. A face is a bounded portion of a surface; a loop is a circuit of edges bounding a face; an edge is a bounded piece of a curve, and a vertex lies at a point.

Figure 13 shows the B-Rep of an X-shape face here taken as a representative example of a portion of the lattice. The X shape has 16 vertices (V_1, V_2,...,V_{16}), 16 edges (E_1, E_2,...,E_{16}), 1 loop (L_1), and 1 face (F_1). When the coordinates of vertices are obtained and expressed through the B-rep topological information, the CAD model can be constructed following the sequence vertex →edge→loop→face. With the fully acquired B-rep representation, complex geometries can be built bottom up. In this study,

Fig. 12 Titanium-based alloy implant with optimized lattice architecture built via SLM

homogenized medium, and hence, its effective properties do not account for the localized stress and strain that can emerge through the interaction between the porous portion of the proximal part of the stem and the adjacent bone tissue. Furthermore, the mechanical properties of the lattice material are calculated under the assumption that the implant domain is infinitely periodic with no boundary effects. In addition, uncertainties that can emerge from a number of sources including unknown origin of the patient bone, variation of bone properties, patient gender, and age, as well as imperfections from manufacturing are not considered. Despite these points, the proof-of-concept implant presented in this paper is promising and warrants an experimental campaign of mechanical testing followed by clinical validation.
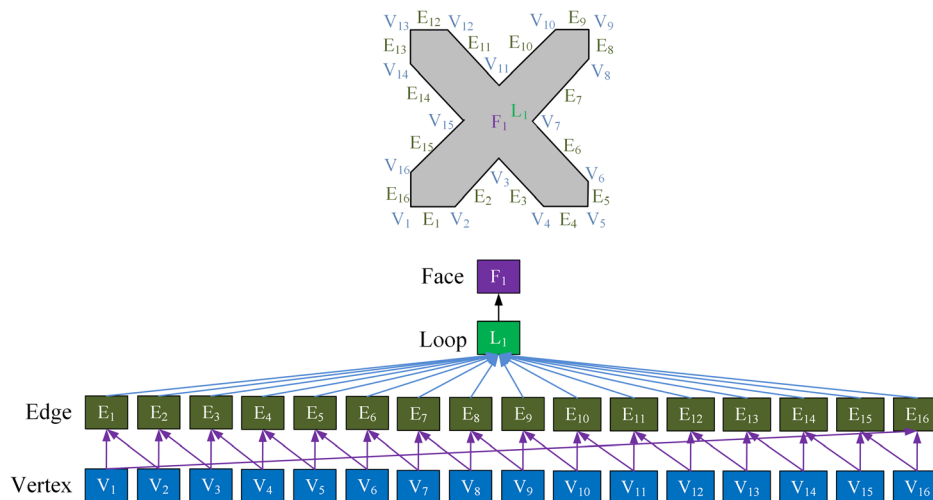
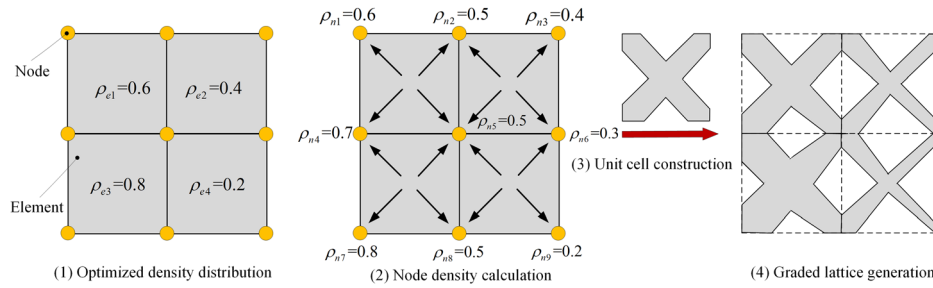**Fig. 13   B-Rep of an X-shape face with 16 vertices**

Fig. 14 Schematic for automatic generation of a graded lattice structure

each mesh element of the finite element model is used to locate the vertices, and a sequence of four steps is implemented to generate the graded lattice (Fig. 14):

(1) *Element density assignment*: The element density denoted by ρ_e is directly obtained from topology optimization and assigned to each unit cell of the lattice.
(2) *Node density calculation*: The node density of an element ρ_n is calculated by averaging the densities of the neighbor elements. From a given node density and node coordinates, the vertices of a unit cell can be obtained.
(3) *Unit cell construction*: The information obtained in Eq. (2) on the vertex coordinates of each unit cell, can be expressed through its B-Rep representation (Fig. 13), from which the unit cell can be constructed. This step is individually repeated for each element of the mesh.
(4) *Lattice generation*: In the last step, Boolean operations are used to combine all the unit cells in the lattice.

Because a computational model in a CAD system is boundary-represented, the above procedure can be automatically implemented to generate a CAD model of a lattice structure.

Appendix B: Influence of the Penalization Factor on the Young's Modulus

The solid isotropic material with penalization scheme is a powerful method to determine the optimal material distribution in a given design space for a given set of loads, boundary conditions and constraints [37,76,77]. It commonly yields to black-white (0/1) solutions, where the elastic modulus of an element $E(\rho_i)$ is given by

$$E(\rho_i) = E_{\min} + \rho_i^p (E_0 - E_{\min}), \quad \rho_i \in [0, 1] \qquad \text{(B1)}$$

where $E_{\min}$ is the stiffness of soft (void) material (typically 10^{-9}), E_0 is the elastic modulus of the solid material, and p is the penalization factor (typically $p = 3$). By selecting a priori the exponent p of Eq. (B1), the relationship between the Young's modulus and the element density is established, although this relation may not necessarily represent the actual constitutive relation of the material. The density distributions are then obtained by applying a penalization factor that might not be representative of the real material. To show this dependency, we solve here a classical compliance problem and compared the results obtained with two methods having different penalization factor.

The problem is the Messerschmitt–Bölkow–Blohm beam (Fig. 15(*a*)), where the objective is to minimize compliance [37,77]. Figure 15(*b*) shows the black-and-white solution obtained with the conventional PTO with a penalty factor of 3 [37], and Fig. 15(*c*) illustrates the gray solution obtained with the density-continuous PTO with a penalty factor of 1. The former is more compliant than the latter (266.61 versus 206.98), which is also faster to obtain (number of iteration: 170 versus 51). The results show that the value of the penalty factor (Eq. (B1)) that is selected a priori has an influence on the relationship between Young's modulus and element density. For this reason, in this work, we do not assume any value for p; rather as described in Sec. 3, we use AH to establish the effective properties of the lattice as a function of the relative density of the unit cell and use these properties in the optimization process.
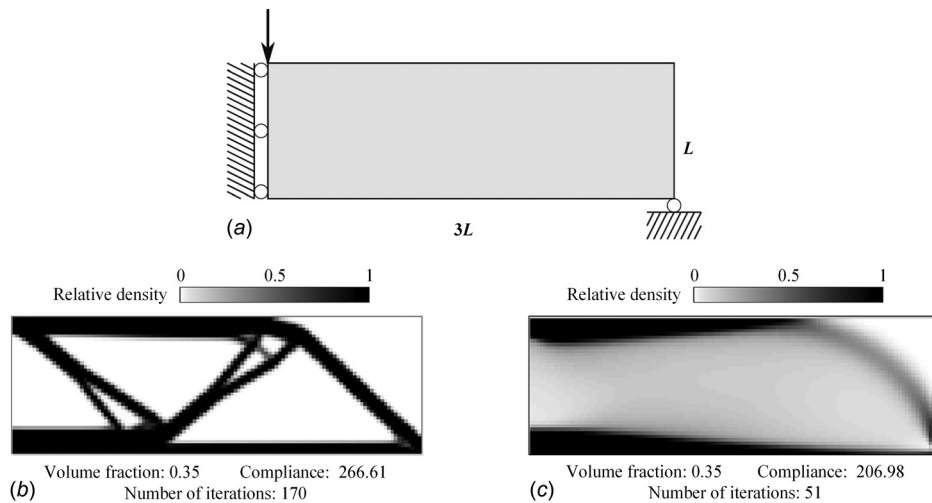

Fig. 15 Optimization of the Messerschmitt–Bölkow–Blohm beam for minimal compliance: (*a*) design domain and boundary conditions, (*b*) black-and-white solution obtained with original PTO [37], and (*c*) gray solution calculate with the density-continuous PTO

References

[1] Pivec, R., Johnson, A. J., Mears, S. C., and Mont, M. A., 2012, "Hip Arthroplasty," Lancet, **380**(9855), pp. 1768–1777.

[2] Iolascon, G., Di Pietro, G., Capaldo, A., Gioia, C., Gatto, S., and Gimigliano, F., 2010, "Periprosthetic Bone Density as Outcome of Therapeutic Response," Clin. Cases Miner. Bone Metabol., **7**(1), pp. 27–31.

[3] Dattani, R., 2007, "Femoral Osteolysis Following Total Hip Replacement," Postgrad. Med. J., **83**(979), pp. 312–316.

[4] Berry, D. J., Harmsen, W. S., Cabanela, M. E., and Morrey, B. F., 2002, "Twenty-Five-Year Survivorship of Two Thousand Consecutive Primary Charnley Total Hip Replacements," J. Bone Jt. Surg. Am., **84**(2), pp. 171–177.

[5] Khanuja, H. S., Vakil, J. J., Goddard, M. S., and Mont, M. A., 2011, "Cementless Femoral Fixation in Total Hip Arthroplasty," J. Bone Jt. Surg. Am., **93**(5), pp. 500–509.

[6] Ridzwan, M. I. Z., Shuib, S., Hassan, A. Y., Shokri, A. A., and Mohamad Ibrahim, M. N., 2007, "Problem of Stress Shielding and Improvement to the Hip Implant Designs: A Review," J. Med. Sci., **7**(3), pp. 460–467.

[7] Mahomed, N. N., Barrett, J. A., Katz, J. N., Phillips, C. B., Losina, E., Lew, R. A., Guadagnoli, E., Harris, W. H., Poss, R., and Baron, J. A., 2003, "Rates and Outcomes of Primary and Revision Total Hip Replacement in the United States Medicare Population," J. Bone Jt. Surg. Am., **85**(1), pp. 27–32.

[8] Kurtz, S., Ong, K., Lau, E., Mowat, F., and Halpern, M., 2007, "Projections of Primary and Revision Hip and Knee Arthroplasty in the United States From 2005 to 2030," J. Bone Jt. Surg., **89**(4), pp. 780–785.

[9] Ulrich, S. D., Seyler, T. M., Bennett, D., Delanois, R. E., Saleh, K. J., Thongtrangan, I., Kuskowski, M., Cheng, E. Y., Sharkey, P. F., and Parvizi, J., 2008, "Total Hip Arthroplasties: What Are the Reasons for Revision?," Int. Orthop., **32**(5), pp. 597–604.

[10] Khanoki, S. A., and Pasini, D., 2012, "Multiscale Design and Multiobjective Optimization of Orthopedic Hip Implants With Functionally Graded Cellular Material," ASME J. Biomech. Eng., **134**(3), p. 031004.

[11] Bougherara, H., Zdero, R., Dubov, A., Shah, S., Khurshid, S., and Schemitsch, E. H., 2011, "A Preliminary Biomechanical Study of a Novel Carbon–Fibre Hip Implant Versus Standard Metallic Hip Implants," Med. Eng. Phys., **33**(1), pp. 121–128.

[12] Simoes, J., and Marques, A., 2005, "Design of a Composite Hip Femoral Prosthesis," Mater. Des., **26**(5), pp. 391–401.

[13] Scholz, M.-S., Blanchfield, J., Bloom, L., Coburn, B., Elkington, M., Fuller, J., Gilbert, M., Muflahi, S., Pernice, M., and Rae, S., 2011, "The Use of Composite Materials in Modern Orthopaedic Medicine and Prosthetic Devices: A Review," Compos. Sci. Technol., **71**(16), pp. 1791–1803.

[14] Evans, S., and Gregson, P., 1998, "Composite Technology in Load-Bearing Orthopaedic Implants," Biomaterials, **19**(15), pp. 1329–1342.

[15] Brandwood, A., Noble, K. R., and Schindhelm, K., 1992, "Phagocytosis of Carbon Particles by Macrophages In Vitro," Biomaterials, **13**(9), pp. 646–648.

[16] Wen, C., Mabuchi, M., Yamada, Y., Shimojima, K., Chino, Y., and Asahina, T., 2001, "Processing of Biocompatible Porous Ti and Mg," Scr. Mater., **45**(10), pp. 1147–1153.

[17] Ryan, G., Pandit, A., and Apatsidis, D. P., 2006, "Fabrication Methods of Porous Metals for Use in Orthopaedic Applications," Biomaterials, **27**(13), pp. 2651–2670.

[18] Pattanayak, D. K., Fukuda, A., Matsushita, T., Takemoto, M., Fujibayashi, S., Sasaki, K., Nishida, N., Nakamura, T., and Kokubo, T., 2011, "Bioactive Ti Metal Analogous to Human Cancellous Bone: Fabrication by Selective Laser Melting and Chemical Treatments," Acta Biomater., **7**(5), pp. 1398–1406.

[19] Cheng, A., Humayun, A., Cohen, D. J., Boyan, B. D., and Schwartz, Z., 2014, "Additively Manufactured 3D Porous Ti–6Al–4V Constructs Mimic Trabecular Bone Structure and Regulate Osteoblast Proliferation, Differentiation and Local Factor Production in a Porosity and Surface Roughness Dependent Manner," Biofabrication, **6**(4), p. 045007.

[20] Li, X., Wang, C., Zhang, W., and Li, Y., 2009, "Fabrication and Characterization of Porous Ti6Al4V Parts for Biomedical Applications Using Electron Beam Melting Process," Mater. Lett., **63**(3–4), pp. 403–405.

[21] Bandyopadhyay, A., Espana, F., Balla, V. K., Bose, S., Ohgami, Y., and Davies, N. M., 2010, "Influence of Porosity on Mechanical Properties and In Vivo Response of Ti6Al4V Implants," Acta Biomater., **6**(4), pp. 1640–1648.

[22] Wang, X., Xu, S., Zhou, S., Xu, W., Leary, M., Choong, P., Qian, M., Brandt, M., and Xie, Y. M., 2016, "Topological Design and Additive Manufacturing of Porous Metals for Bone Scaffolds and Orthopaedic Implants: A Review," Biomaterials, **83**, pp. 127–141.

[23] Kuiper, J. H., and Huiskes, R., 1997, "Mathematical Optimization of Elastic Properties: Application to Cementless Hip Stem Design," ASME J. Biomech. Eng., **119**(2), pp. 166–174.

[24] Kuiper, J. H., and Huiskes, R., 1992, "Numerical Optimization of Hip-Prosthetic Stem Material," Recent Advances in Computer Methods in Biomechanics and Biomedical Engineering, J. Middleton, G. N. Pande, and K. R. Williams, eds., Books and Journals International, Ltd., Swansea, UK, pp. 76–84.

[25] Gross, S., and Abel, E. W., 2001, "A Finite Element Analysis of Hollow Stemmed Hip Prostheses as a Means of Reducing Stress Shielding of the Femur," J. Biomech., **34**(8), pp. 995–1003.

[26] Hedia, H. S., Shabara, M. A. N., EI-Midany, T. T., and Fouda, N., 2006, "Improved Design of Cementless Hip Stems Using Two-Dimensional Functionally Graded Materials," J. Biomed. Mater. Res. B., **79**(1), pp. 42–49.

[27] Fraldi, M., Esposito, L., Perrella, G., Cutolo, A., and Cowin, S. C., 2010, "Topological Optimization in Hip Prosthesis Design," Biomech. Model. Mech., **9**(4), pp. 389–402.

[28] Kayabasi, O., and Ekici, B., 2007, "The Effects of Static, Dynamic and Fatigue Behavior on Three-Dimensional Shape Optimization of Hip Prosthesis by Finite Element Method," Mater. Des., **28**(8), pp. 2269–2277.

[29] Higa, M., Tanino, H., Nishimura, I., Mitamura, Y., Matsuno, T., and Ito, H., 2015, "Three-Dimensional Shape Optimization of a Cemented Hip Stem and Experimental Validations," J. Artif. Organs, **18**(1), pp. 79–85.

[30] Rungsiyakull, C., Li, Q., Sun, G., Li, W., and Swain, M. V., 2010, "Surface Morphology Optimization for Osseointegration of Coated Implants," Biomaterials, **31**(27), pp. 7196–7204.

[31] Lin, D., Li, Q., Li, W., Zhou, S., and Swain, M. V., 2009, "Design Optimization of Functionally Graded Dental Implant for Bone Remodeling," Compos. Part B: Eng, **40**(7), pp. 668–675.

[32] Chen, J., Rungsiyakull, C., Li, W., Chen, Y., Swain, M., and Li, Q., 2013, "Multiscale Design of Surface Morphological Gradient for Osseointegration," J. Mech. Behav. Biomed. Mater, **20**, pp. 387–397.

[33] Khanoki, S. A., and Pasini, D., 2013, "Fatigue Design of a Mechanically Biocompatible Lattice for a Proof-of-Concept Femoral Stem," J. Mech. Behav. Biomed. Mater, **22**, pp. 65–83.

[34] Arabnejad, S., Johnston, R. B., Pura, J. A., Singh, B., Tanzer, M., and Pasini, D., 2016, "High-Strength Porous Biomaterials for Bone Replacement: A Strategy to Assess the Interplay Between Cell Morphology, Mechanical Properties, Bone Ingrowth and Manufacturing Constraints," Acta Biomater., **30**, pp. 345–356.

[35] Melancon, D., Bagheri, Z., Johnston, R., Liu, L., Tanzer, M., and Pasini, D., 2017, "Mechanical Characterization of Structurally Porous Biomaterials Built Via Additive Manufacturing: Experiments, Predictive Models, and Design Maps for Load-Bearing Bone Replacement Implants," Acta Biomater., **63**, pp. 350–368.

[36] Deb, K., Pratap, A., Agarwal, S., and Meyarivan, T., 2002, "A Fast and Elitist Multiobjective Genetic Algorithm: NSGA-II," IEEE T. Evolut. Comput., **6**(2), pp. 182–197.

[37] Biyikli, E., and To, A. C., 2015, "Proportional Topology Optimization: A New Non-Sensitivity Method for Solving Stress Constrained and Minimum Compliance Problems and Its Implementation in MATLAB," PloS One, **10**(12), p. e0145041.

[38] Rozvany, G. I., Zhou, M., and Birker, T., 1992, "Generalized Shape Optimization Without Homogenization," Struct. Optim., **4**(3-4), pp. 250–252.

[39] Bendsøe, M. P., and Sigmund, O., 1999, "Material Interpolation Schemes in Topology Optimization," Arch. Appl. Mech., **69**(9–10), pp. 635–654.

[40] Bendsøe, M. P., and Sigmund, O., 2003, Topology Optimization: Theory, Methods, and Applications, Springer, Berlin.

[41] Jensen, K. E., 2016, "Anisotropic Mesh Adaptation and Topology Optimization in Three Dimensions," ASME J. Mech. Des., **138**(6), p. 061401.

[42] Allaire, G., Jouve, F., and Toader, A.-M., 2004, "Structural Optimization Using Sensitivity Analysis and a Level-Set Method," J. Comput. Phys., **194**(1), pp. 363–393.

[43] Wang, M. Y., Wang, X., and Guo, D., 2003, "A Level Set Method for Structural Topology Optimization," Comput. Methods Appl. Mech. Eng, **192**(1–2), pp. 227–246.

[44] Deng, X., Wang, Y., Yan, J., Liu, T., and Wang, S., 2016, "Topology Optimization of Total Femur Structure: Application of Parameterized Level Set Method Under Geometric Constraints," ASME J. Mech. Des., **138**(1), p. 011402.

[45] Liu, J., and Ma, Y., 2017, "Sustainable Design-Oriented Level Set Topology Optimization," ASME J. Mech. Des., **139**(1), p. 011403.

[46] Svanberg, K., 1987, "The Method of Moving Asymptotes—A New Method for Structural Optimization," Int. J. Numer. Methods Eng., **24**(2), pp. 359–373.

[47] Egan, P. F., Ferguson, S. J., and Shea, K., 2017, "Design of Hierarchical Three-Dimensional Printed Scaffolds Considering Mechanical and Biological Factors for Bone Tissue Engineering," ASME J. Mech. Des., **139**(6), p. 061401.

[48] Arabnejad, S., Johnston, B., Tanzer, M., and Pasini, D., 2017, "Fully Porous 3D Printed Titanium Femoral Stem to Reduce Stress-Shielding Following Total Hip Arthroplasty," J. Orthop. Res., **35**(8), pp. 1774–1783.

[49] Bagheri, Z. S., Melancon, D., Liu, L., Johnston, R. B., and Pasini, D., 2017, "Compensation Strategy to Reduce Geometry and Mechanics Mismatches in Porous Biomaterials Built With Selective Laser Melting," J. Mech. Behav. Biomed. Mater, **70**, pp. 17–27.

[50] Shan, Z., and Gokhale, A. M., 2002, "Representative Volume Element for Non-Uniform Micro-Structure," Comput. Mater. Sci., **24**(3), pp. 361–379.

[51] Arabnejad, S., and Pasini, D., 2013, "Mechanical Properties of Lattice Materials Via Asymptotic Homogenization and Comparison With Alternative Homogenization Methods," Int. J. Mech. Sci., **77**, pp. 249–262.

[52] Hollister, S. J., and Kikuchi, N., 1992, "A Comparison of Homogenization and Standard Mechanics Analyses for Periodic Porous Composites," Comput. Mech., **10**(2), pp. 73–95.

[53] Cameron, A. C., and Windmeijer, F. A., 1997, "An R-Squared Measure of Goodness of Fit for Some Common Nonlinear Regression Models," J. Econom., **77**(2), pp. 329–342.

[54] Pidaparti, R., and Turner, C., 1997, "Cancellous Bone Architecture: Advantages of Nonorthogonal Trabecular Alignment Under Multidirectional Joint Loading," J. Biomech., **30**(9), pp. 979–983.

[55] Jang, I. G., and Kim, I. Y., 2009, "Computational Simulation of Trabecular Adaptation Progress in Human Proximal Femur During Growth," J. Biomech., **42**(5), pp. 573–580.

[56] Tsai, S. W., and Wu, E. M., 1971, "A General Theory of Strength for Anisotropic Materials," J. Compos. Mater., **5**(1), pp. 58–80.

[57] Austman, R. L., Milner, J. S., Holdsworth, D. W., and Dunning, C. E., 2008, "The Effect of the Density–Modulus Relationship Selected to Apply Material Properties in a Finite Element Model of Long Bone," J. Biomech., **41**(15), pp. 3171–3176.

[58] Wirtz, D. C., Schiffers, N., Pandorf, T., Radermacher, K., Weichert, D., and Forst, R., 2000, "Critical Evaluation of Known Bone Material Properties to Realize Anisotropic FE-Simulation of the Proximal Femur," J. Biomech., **33**(10), pp. 1325–1330.

[59] Heller, M., Bergmann, G., Kassi, J.-P., Claes, L., Haas, N., and Duda, G., 2005, "Determination of Muscle Loading at the Hip Joint for Use in Pre-Clinical Testing," J. Biomech., **38**(5), pp. 1155–1163.

[60] Speirs, A. D., Heller, M. O., Duda, G. N., and Taylor, W. R., 2007, "Physiologically Based Boundary Conditions in Finite Element Modelling," J. Biomech., **40**(10), pp. 2318–2323.

[61] Sperati, G., and Ceri, L., 2014, "Total Hip Arthroplasty Using TRI-LOCK® DePuy Bone Preservation Femoral Stem: Our Experience," Acta Biomed., **85**(2), pp. 66–70.

[62] Burt, C. F., Garvin, K. L., Otterberg, E. T., and Jardon, O. M., 1998, "A Femoral Component Inserted Without Cement in Total Hip Arthroplasty. A Study of the Tri-Lock Component With an Average Ten-Year Duration of Follow-Up*," J. Bone Jt. Surg., **80**(7), pp. 952–960.

[63] Cuppone, M., Seedhom, B. B., Berry, E., and Ostell, A. E., 2004, "The Longitudinal Young's Modulus of Cortical Bone in the Midshaft of Human Femur and Its Correlation With CT Scanning Data," Calcif. Tissue Int., **74**(3), pp. 302–309.

[64] Sigmund, O., 2001, "A 99 Line Topology Optimization Code Written in MATLAB," Struct. Multidiscip. Optim., **21**(2), pp. 120–127.

[65] Eschenauer, H. A., and Olhoff, N., 2001, "Topology Optimization of Continuum Structures: A Review*," ASME Appl. Mech. Rev., **54**(4), pp. 331–390.

[66] Harrysson, O. L., Cansizoglu, O., Marcellin-Little, D. J., Cormier, D. R., and West, H. A., 2008, "Direct Metal Fabrication of Titanium Implants With Tailored Materials and Mechanical Properties Using Electron Beam Melting Technology," Mater. Sci. Eng. C: Mater., **28**(3), pp. 366–373.

[67] de Wild, M., Schumacher, R., Mayer, K., Schkommodau, E., Thoma, D., Bredell, M., Kruse Gujer, A., Grätz, K. W., and Weber, F. E., 2013, "Bone Regeneration by the Osteoconductivity of Porous Titanium Implants Manufactured by Selective Laser Melting: A Histological and Micro Computed Tomography Study in the Rabbit," Tissue Eng. Part A, **19**(23–24), pp. 2645–2654.

[68] Kowalczyk, P., 2001, "Design Optimization of Cementless Femoral Hip Prostheses Using Finite Element Analysis," ASME J. Biomech. Eng., **123**(5), pp. 396–402.

[69] Harvey, E., Bobyn, J., Tanzer, M., Stackpool, G., Krygier, J., and Hacking, S., 1999, "Effect of Flexibility of the Femoral Stem on Bone-Remodeling and Fixation of the Stem in a Canine Total Hip Arthroplasty Model Without Cement," J. Bone Jt. Surg. Am., **81**(1), pp. 93–107.

[70] Weinans, H., Huiskes, R., and Grootenboer, H. J., 1992, "Effects of Material Properties of Femoral Hip Components on Bone Remodeling," J. Orthop. Res, **10**(6), pp. 845–853.

[71] Huang, X., and Xie, Y., 2007, "Convergent and Mesh-Independent Solutions for the Bi-Directional Evolutionary Structural Optimization Method," Finite Elem. Anal. Des, **43**(14), pp. 1039–1049.

[72] Murr, L., Gaytan, S., Medina, F., Lopez, H., Martinez, E., Machado, B., Hernandez, D., Martinez, L., Lopez, M., and Wicker, R., 2010, "Next-Generation Biomedical Implants Using Additive Manufacturing of Complex, Cellular and Functional Mesh Arrays," Philos. Trans. R. Soc. A: Math. Phys. Eng. Sci., **368**(1917), pp. 1999–2032.

[73] Heinl, P., Müller, L., Körner, C., Singer, R. F., and Müller, F. A., 2008, "Cellular Ti–6Al–4V Structures With Interconnected Macro Porosity for Bone Implants Fabricated by Selective Electron Beam Melting," Acta Biomater., **4**(5), pp. 1536–1544.

[74] Liu, L., Kamm, P., García-Moreno, F., Banhart, J., and Pasini, D., 2017, "Elastic and Failure Response of Imperfect Three-Dimensional Metallic Lattices: The Role of Geometric Defects Induced by Selective Laser Melting," J. Mech. Phys. Solids, **107**, pp. 160–184.

[75] Babic, B., Nesic, N., and Miljkovic, Z., 2008, "A Review of Automated Feature Recognition With Rule-Based Pattern Recognition," Comput. Ind., **59**(4), pp. 321–337.

[76] Sigmund, O., 2007, "Morphology-Based Black and White Filters for Topology Optimization," Struct. Multidiscip. Optim., **33**(4–5), pp. 401–424.

[77] Andreassen, E., Clausen, A., Schevenels, M., Lazarov, B. S., and Sigmund, O., 2011, "Efficient Topology Optimization in MATLAB Using 88 Lines of Code," Struct. Multidiscip. Optim., **43**(1), pp. 1–16.